PHASE ANGLE EFFECT ON HEAT TRANSFER AND INDICATED POWER OF FREE PISTON STIRLING ENGINE

***Umair MUNIR*[*1], *Syed Murawat Abbas NAQVI*[1], *Muhammad Yasar JAVAID*[2], *Muhammad WAQAS*[3], *Hafiz Muhammad WAQAS*[1]**

[*1]Mechanical Engineering Department, NFC IEFR, Faisalabad, Pakistan

[2]Department of Mechanical Engineering Technology, Government College University, Faisalabad, Pakistan

[3]Department of Mechanical Engineering, University of Sargodha, Sargodha, Pakistan

[*] Corresponding author; E-mail: umair.munir1@gmail.com, umair_munir@iefr.edu.pk

In this work, a transient CFD analysis is performed to analyze the effects posed by changing the phase angle between the displacer and power piston in a free piston Stirling engine. The numerical model that is used for analysis is axisymmetric which contains live engine spaces (expansion and compression space) and dead spaces (heater, regenerator, and cooler). The displacer and power piston movements are defined by a user defined function. The results showed that the compression ratio and pressure wave amplitude are strong function of phase angle and peaked at 120^o phase angle. The optimum phase angle is also changing with operating frequency. The suitable phase angle at 80 Hz is the range of 60^o-70^o, but at a lower frequency around 50 Hz, its range is 80^o-100^o. The results also showed that the heat transfer rate at the heater and cooler channels are influenced by the change of phase angle. The heat exchange at the heater and cooler is peaked at 90° and 100° phase angle respectively. The flow losses from the heater, regenerator and cooler showed a rising trend with phase angle increase. The optimum phase angle was obtained by making a balance between phase angle effects and found the optimum range to be between 60°- 80° for peak power and efficiency.

Key words*: Free piston Stirling engine, CFD, Phase angle*

1. Introduction

Free piston Stirling engines (FPSEs) are externally heated engines that are used to generate electricity from solar or any low-graded heat source. This engine is free of crankshaft and directly converts the linear motion of piston into electricity by using linear alternators. The FPSE arrangement is preferred because it has minimum moving parts and has shown maintenance free unattended long operation capabilities. The application of the Stirling engine ranges from solar power generation [1] by using a parabolic trough collector [2], combined heat and power systems [3], [4], [5], space power generation [6], micro-cogeneration [7] and waste heat recovery [8], [9]. FPSE works on the Stirling

cycle and commonly uses air, hydrogen or helium as working gas, which oscillates between hot expansion space and cold compression space through an annular heater, cooler and regenerator. [10].

Recently, Rabhi et al. [11] evaluated the performance of concentrated solar power plant based on Stirling engine and proposed optimal configuration of heat exchangers, and regenerators. Salazar and Chen [12] used an axisymmetric CFD model for the analysis of a beta type rhombic drive Stirling engine and it was found that the heat transfer coefficient was not constant with time and space. Chen et al. [13] investigated the effect of moving regenerator on the heat transfer process of beta type Stirling engine. Laminar flow and thermal equilibrium model for regenerator were assumed and it was found that maximum efficiency was at 99 percent porosity. In another study, Chen et al. [14] investigated the effect of some geometric parameters of low temperature differential twin power piston gamma type prototype engine and found that piston stroke, piston diameter and engine speed had a positive impact on power and efficiency.

A numerical analysis was performed for 1kW beta type Stirling engine by Cheng and Chen [15] and it was concluded that the optimum regenerator porosity was 90 % with helium as working gas due to low viscosity and high thermal conductivity. Xiao et al. [16] compared an improved simple analytical model and CFD model for beta type Stirling engine prototype. The effect of dead volume and heat transfer area of the heater was investigated and the redesign of heater resulted in 1.6 percent improvement in efficiency. A parametric study was performed by Abuelaymen et al. [17] for rhombic drive beta type Stirling and investigated the effect of working gas. Almajri et al. [18] compared non-ideal adiabatic thermodynamic and CFD models for parametric study of alpha type Stirling engine. In the most recent studies, Kuban et al. [19] studied the complexity of flow and turbulence characteristics by using a multidimensional CFD method validated with the ST05G engine. Caetano et al. [20] used the discrete ordinates (DO) radiation model and displacer temperature boundary condition in CFD simulation to further reduce the error in performance prediction of a beta type Stirling engine prototype. A 3D CFD model was presented by El-Ghafour et al. [21] for the GPU-3 engine to analyze the cyclic thermal and flow fields and to find the most appropriate turbulence model.

Alfarawi et al. [22] evaluated the effect of phase angle on engine indicated power and transient variations of temperature and pressure were analyzed to optimize the dead volume of the connecting pipe. The transient CFD simulation was performed for the gamma-type Stirling engine and it was found that at 105° the power was maximum with minimum losses.

It was observed during the literature survey that there has been limited work published in the field of numerical modeling of free piston Stirling engines based on the CFD method and none of the CFD model included piston seal losses into account. Furthermore, most of the CFD models developed without heat exchanger incorporated in the model. In this work, authors used the an axisymmetric CFD model for a 12.5 kW Component Test Power Converter (CTPC) [23] to analyze the effect of phase angle on engine performance. In the current study, the effect of phase angle on indicated power, efficiency, heat transfer rate and flow losses is presented.

2. Numerical modelling

The Stirling engine that is used in this study was built for space power application. Complete engine geometric details and operating conditions are given in the literature [24]. The computational domain was built by utilizing the engine's live volumes in expansion and compression spaces. These volumes were changing due to the reciprocating motion of the two pistons housed in the same

cylinder. The initial positions of the displace and power piston were set to be at mid-stroke and BDC respectively. The heater, cooler and regenerator were built by matching the dead volumes, channel hydraulic diameters, channel lengths and heat transfer area.

The computation domain that is used in the current study is presented in Fig. 1. The boundary walls are categorized into symmetric, moving, and isothermal walls.

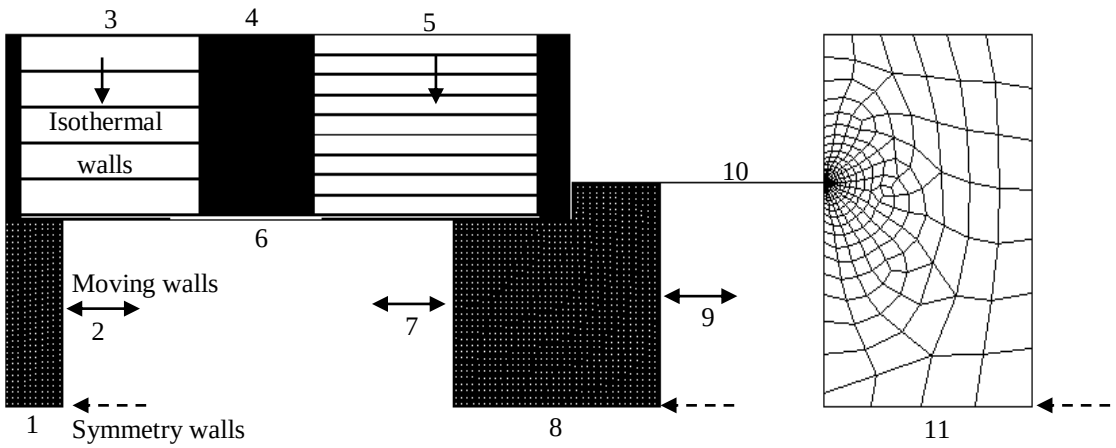

Fig. 1 Types of boundary walls and engine components 1. Expansion space 2. Moving displacer wall (upper) 3. Heater 4. Regenerator 5. Cooler 6. Displacer seal 7. Moving displacer wall (lower) 8. Compression Space 9. Moving Piston wall 10. Piston seal 11. Bounce space

2.1. Model validation, mesh and time sensitivity analysis

The governing equations and the numerical model are presented in our previous work [23] with complete geometric details and operating conditions are given. The developed model was validated against the experimental data presented in [24] and [25]. Fig. 2 compares the indicated power as function of displacer amplitude for experimental engine (CTPC) and numerical values. The mesh sensitivity was also checked by using three different meshes coarse, medium and fine meshes having 74649, 96508 and 162048 cells respectively. The medium mesh with 96508 element was selected for further analysis because the variation in power output by using medium and fine mesh was below 1 %. Time step sensitivity analysis was also performed by comparing the data obtained from 360, 180 and 90-time steps/cycle were compared and it was found that 360 time steps per cycle showed better convergence and accuracy of results.

3. Results and discussion

3.1. Cyclic thermal and flow fields

This section explains the cyclic variation of pressure and volume, after reaching steady state in 30^{th} working cycle. The volume variation of expansion space and compression space is presented in Fig. 3, which is due to displacer and piston movement. The phase difference between the piston and displacer was set at 70.83° taken from experiment [24]. Instantaneous pressures of expansion and compression space obtained from simulation are also plotted in Fig. 3. It is observed that the pressure wave is more closely linked to piston movement rather than displacer. Pressure wave is peaked when piston has passed its TDC position having -12° phase difference. The maximum and minimum

pressure is observed during one complete cycle were 17.1 MPa at 172° crank angle and 13.68 MPa at 352° crank angle in compression space.

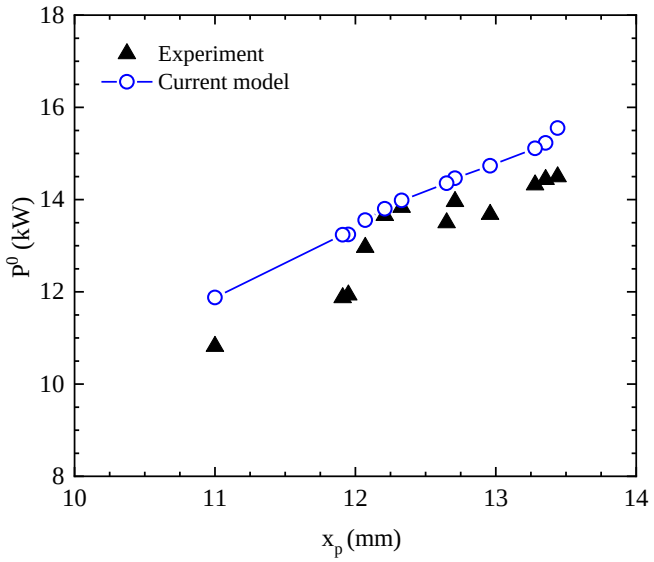

Fig. 2 Indicated power at different displacer amplitudes at 67.45 Hz (model validation)

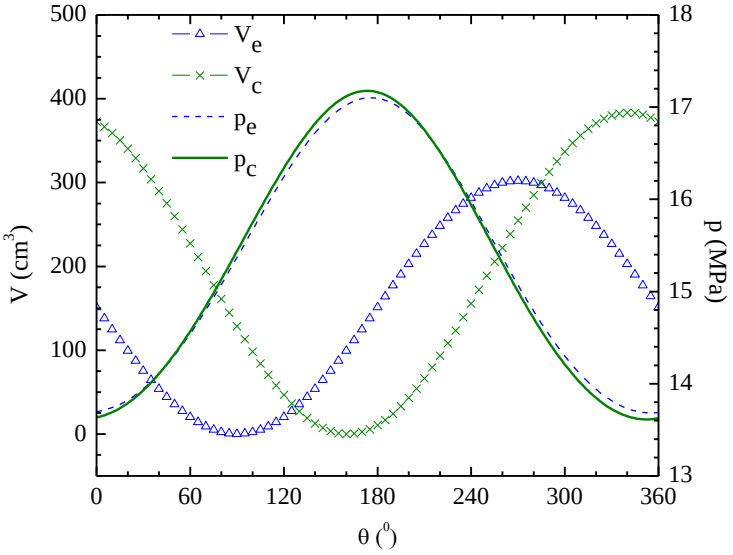

Fig. 3 Instantaneous pressure and volume variation of engine expansion and compression spaces

Separate pressure volume diagrams for expansion space and compression space were plotted in order to find net indicated work of one complete working cycle. The area enclosed in each curve is calculated by integrating PV curve by using Eq. (1) or by Riemann sums method.

$$w_{net} = w_e - w_c = \oint p_e dV_e - \oint p_c dV_c \qquad (1)$$

The indicated power was evaluated by multiplying net work done in one cycle and total number of cycles completed in one second (frequency) by using Eq. (2). Indicated efficiency was

found by Eq. (3) in which, Q_{in} is the amount of heat added through heater wall, which was found by integrating heat flux over the area of the heater wall by using Eq. (4). Similarly, heat transfer rate at cooler Q_{out} and net heat transfer rate Q_{net} was found by Eq. (5)

$$P^0 = w_{net} \times f \tag{2}$$

$$\eta_{ind} = \frac{P^0}{Q_{in}} \tag{3}$$

$$Q_{in} = \iint Q_h^{'} dA_h \tag{4}$$

$$Q_{net} = Q_{in} - Q_{out} = \iint Q_h^{'} dA_h - \iint Q_k^{'} dA_k \tag{5}$$

The flow of working gas inside FPSE is oscillatory and flow direction is reversing through heater and cooler channels twice during the cycle. At each flow reversal, the flow rate of gas in heat exchangers is minimized. The viscous and inertial flow losses were calculated separately for heater, regenerator and cooler and results are presented in Fig. 4 for cold blow. In cold blow, the gas is transported from compression space to expansion space. The pressure loss across heater and cooler channels is due to wall friction and strongly affected by velocity variation of gas. The pressure drop across regenerator is due to viscous and inertial resistances. It is observed that the losses are peaked in the middle of cold blow when axial velocities are higher. But at the flow reversal, the velocity of gas is minimized so as the pressure loss.

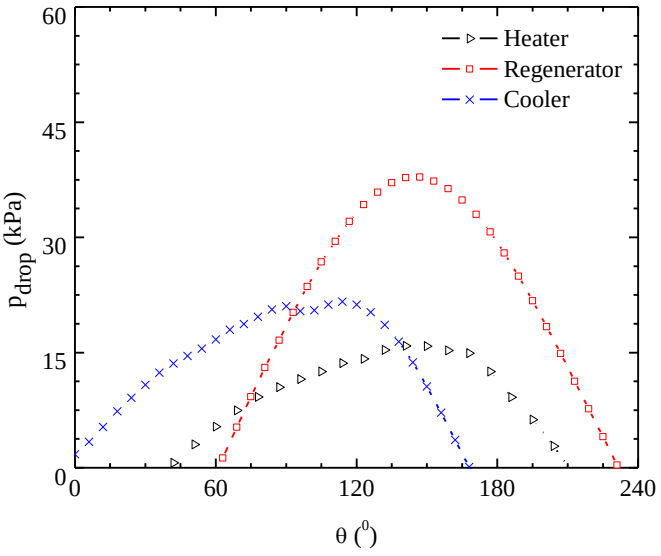

Fig. 4 Instantaneous pressure drop across heater, regenerator and cooler during cold blow

In Fig. 5, the contours of temperature for the whole engine are presented. It is noticed that the temperature of gas inside expansion and compression spaces is not uniform due to limited time of mixing of flow jets entering and leaving these spaces during the cycle. The mixing of gas is due to chaotic flow near moving walls forming vortices. The minimum temperature of 410 K is observed in

compression space at beginning of the compression process when the piston is at BDC as shown in Fig. 5(a). The gas started to move to hot side from cold compression space during compression process as the piston moved towards TDC, which resulted in overall rise in temperature and pressure of engine as shown in Fig. 5(b). The piston moved to TDC at the end of compression process which resulted in further rise in temperature and pressure of the engine and maximum temperature of 788 K is noticed in expansion space as shown in Fig. 5(c). The expansion process started as the piston is moved to its mid stroke position from TDC and displacer is moved to BDC from mid stroke. At this point the working gas reversed its direction again from hot to cold side and blown back into compression space reducing the average temperature of compression space as shown in Fig. 5(d).

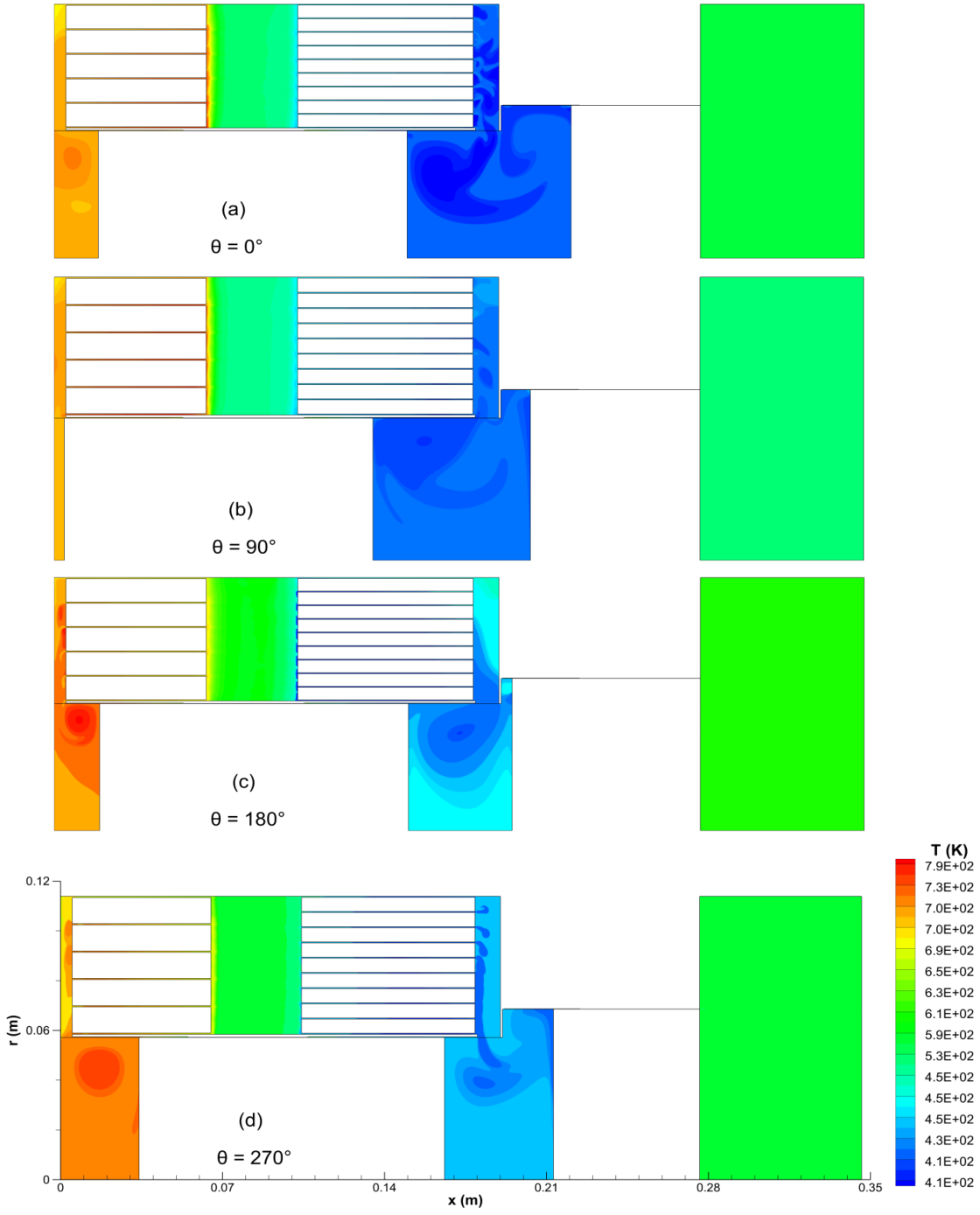

Fig. 5 Temperature contour at four different crank angles during 30th cycle (time = 0.44477 sec)

3.2. Optimization of phase angle

In this section, the effect of phase angle on engine performance is investigated under default operating conditions. Selection of optimum phase angle is critically important because it has significant impact on amplitude of pressure wave, compression ratio, heat transfer rate, pressure losses and hence engine output power and efficiency.

In order to investigate the effect of phase angle, the stroke position of piston is set according to its phase difference from displacer; however, displacer is kept fixed at its mid stroke. The motion of displacer and piston is controlled by compiling individual UDF for each phase angle configuration. The variation of phase angle is affecting compression space volume, which is plotted in Fig. 6. It is noticed that the compression ratio was increasing with phase angle. The maximum and minimum compression ratios are observed at 120° and 50° phase angle respectively. Engine pressure waves generated at different phase angle are also plotted in Fig. 7. It is witnessed that amplitude of the pressure wave is increasing with phase angle. This increase in the amplitude was due to rising compression ratio of the engine. It can be seen that there was approximately 9° phase shift between the consecutive peaks of pressure wave, which was due to time delay of piston to reach its TDC. The pressure wave generated at 120° phase angle had the maximum amplitude.

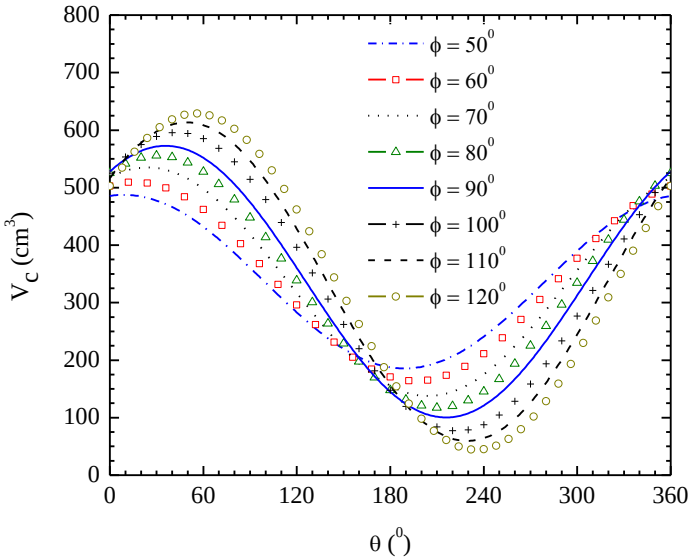

Fig. 6 Cyclic variation of compression space volume at different phase angles

The effect of phase angle on indicated power at different operating frequencies is presented in Fig. 8. It can be observed that optimum phase angle does not remain the same as the frequency is increased. The results are obtained at frequencies of 50 Hz to 80 Hz and optimum phase angle having peak power is decreasing with operating frequency. The effect of phase angle is significant on heat transfer rate, pressure drop and pressure amplitude and peak power was obtained due to balance between these phase angle effects.

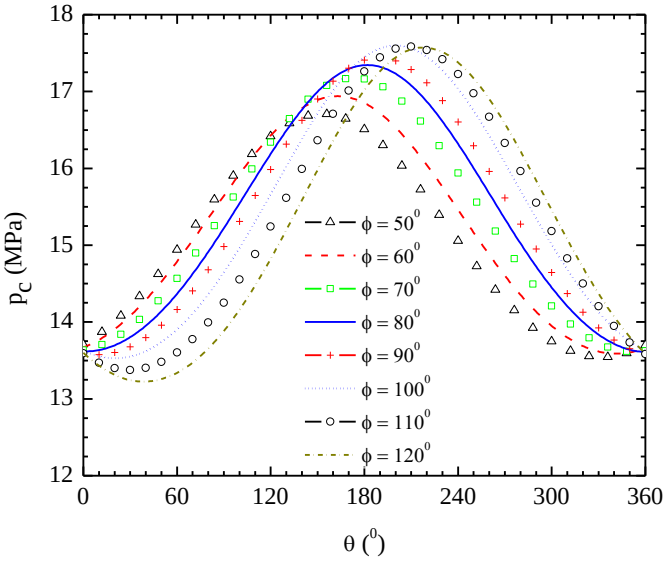

Fig. 7 Cyclic variation of compression space pressure at different phase angles

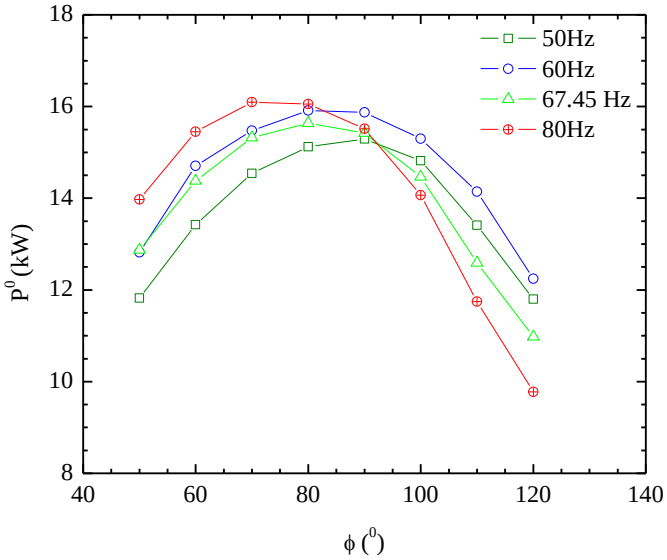

Fig. 8 Effect of phase angle on indicated power at different frequencies

In Fig. 9, the effect of phase angle on engine efficiency at different frequencies is also presented. Efficiency is calculated by dividing indicated power and amount of heat added at heater during one cycle. It is evident that the efficiency was low at higher frequencies, which is due to increased flow losses at higher frequencies. It is also observed that the phase angle having peak efficiency is decreasing as the frequency is increased. The maximum power at different frequencies is reported in the range of 70° to 90° phase angle. However, peak efficiency is obtained at 60° to 80° phase angles.

In Fig. 10, pressure loss and pressure wave amplitude variation with phase angle is presented at 67.45 Hz. It can be seen that both of the parameters are increasing with phase angle. The increase in amplitude of pressure wave is due to rising compression ratio of the engine. However, higher flow

losses are due to increase in turbulence. The turbulent kinetic energy and turbulent viscosity of the gas are increased due to larger swept volumes of compression space. The increase in the amplitude of pressure wave has a positive impact on power output; whereas increase in flow losses is affecting the engine performance negatively. Therefore, the optimum phase angle could be found by balancing these effects.

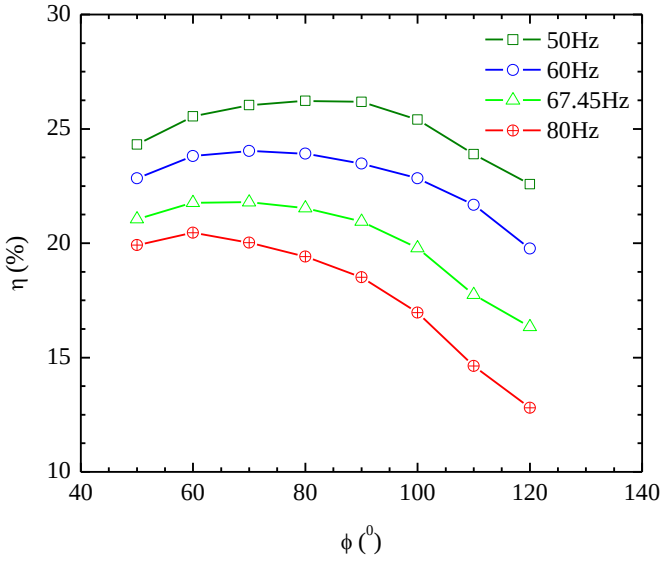

Fig. 9 Effect of phase angle on efficiency at different frequencies

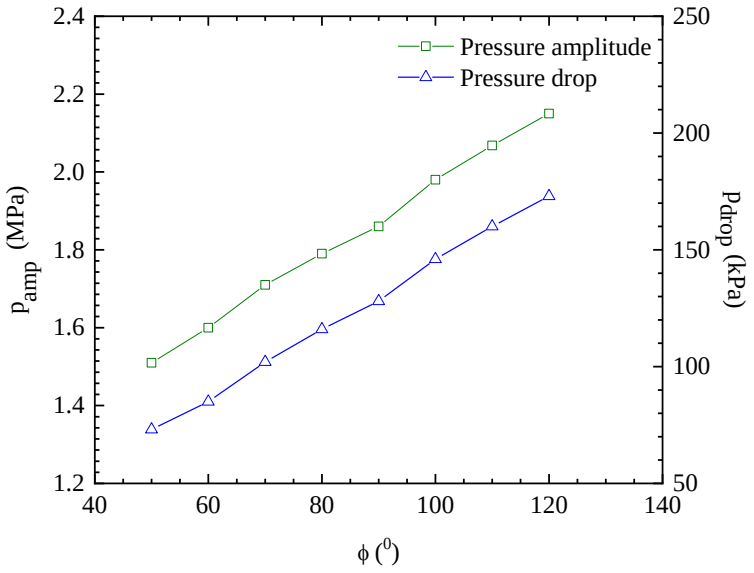

Fig. 10 Effect of phase angle on pressure amplitude and pressure drop

Phase angle effect on heat transfer at heater wall and cooler wall is computed at 67.45 Hz and results are presented in Fig. 11. The results showed that the heat exchange at heater and cooler is peaked at 90° and 100° phase angle respectively. Heat transfer rate is increasing with phase angle initially due to rising gas flow rate and turbulence in heater and cooler channels. However further rise in heat transfer rate is limited due to time delay of expansion and compression process. The increase in

turbulence with phase angle enhanced heat transfer rate as well as flow losses. The output power is directly related to heating power whereas; efficiency is inversely related. This is the reason that the maximum efficiency is reported at 60° phase angle. However, the heart transfer rate at cooler is affecting the power and efficiency in a positive manner. Therefore, peak power is achieved at 80° phase angle, which is due to greater heat transfer rate at heater and cooler, but further rise in power is limited due to increased flow losses. The optimum phase angle is found in the range of 60° to 80° having peak power and efficiency.

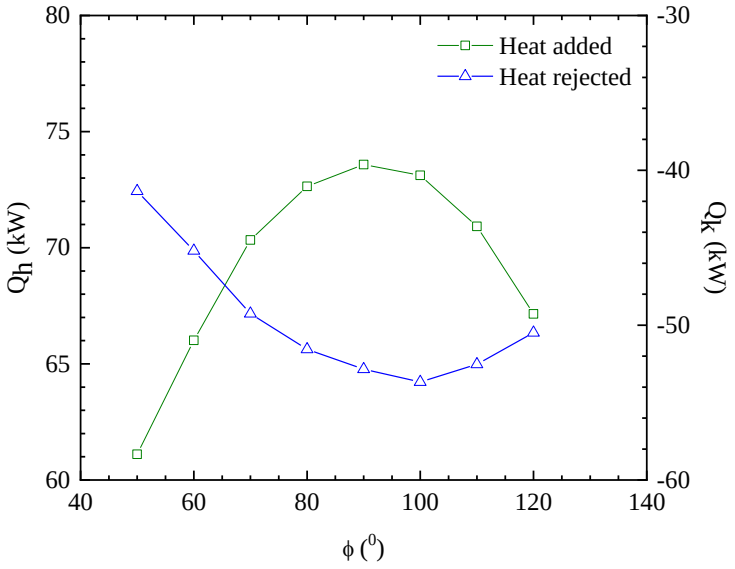

Fig. 11 Effect of phase angle on heating and cooling power

4. Conclusions

The axisymmetric CFD model of FPSE is used to analyze the effect of phase angle on engine performance and heat transfer. It is found from the results that the compression ratio is maximized at 120° and minimized at 50° phase angle. As a result, the amplitude of the pressure wave inside the compression space rises and reaches its peak at 120° phase angle. It was also observed that the phase angles for peak power and efficiency are changing due to frequency. A phase angle of 60°-70° is preferable at 80 Hz and at lower frequencies around 50 Hz, the phase angle of 80°-100° is best suited. The maximum heat transfer rate at the heater and cooler was observed at 90° and 100° phase angle respectively.

The results also showed that the heat exchange at the heater and cooler peaked at 90° and 100° phase angle respectively. However, increased pressure losses with phase angle limited the net power. Maximum power and efficiency were achieved at 80° and 60° phase angles respectively. It is found that engine performance is strongly influenced by phase angle and the phase angle significantly affects heat transfer rate, pressure drop, pressure wave amplitude efficiency, and power.

Nomenclature

f	frequency [Hz]	***Subscript***	
P^0	indicated power, [kW]	*amp*	amplitude

p	pressure, [MPa]	e	expansion space
Q	heat transfer rate, [kW]	c	compression space
V	volume, [cm^3]	k	cooler
w	work done [joule]	h	heater
Greek symbols		d	displacer
θ	crank angle, [°]	p	piston
η	Efficiency		
ϕ	phase angle, [°]		

References

[1] A. Sharma, S. Kumar Shukla, and A. K. Rai, "FINITE TIME THERMODYNAMIC ANALYSIS AND OPTIMIZATION OF SOLAR-DISH STIRLING HEAT ENGINE WITH REGENERATIVE LOSSES," *doiserbia.nb.rs*, vol. 15, no. 4, pp. 995–1009, 2011, doi: 10.2298/TSCI1104181015S.

[2] A. Nattappan, S. P. Ganesan, V. Thiagarajan, and K. Ranganathan, "Design of Automation Control Thermal System Integrated with Parabolic Trough Collector Based Solar Plant," *Thermal Science*, vol. 26, no. 2, 2022, doi: 10.2298/TSCI201113218N.

[3] C. Ulloa, J. L. Míguez, J. Porteiro, P. Eguía, and A. Cacabelos, "Development of a transient model of a stirling-based CHP system," *Energies (Basel)*, vol. 6, no. 7, pp. 3115–3133, 2013, doi: 10.3390/en6073115.

[4] I. Arashnia, G. Najafi, B. Ghobadian, T. Yusaf, R. Mamat, and M. Kettner, "Development of Micro-scale Biomass-fuelled CHP System Using Stirling Engine," in *Energy Procedia*, Elsevier Ltd, 2015, pp. 1108–1113. doi: 10.1016/j.egypro.2015.07.505.

[5] I. W. Eames, K. Evans, and S. Pickering, "A comparative study of open and closed heat-engines for small-scale CHP applications," *Energies (Basel)*, vol. 9, no. 3, Mar. 2016, doi: 10.3390/en9030130.

[6] S. Fan, M. Li, S. Li, T. Zhou, Y. Hu, and S. Wu, "Thermodynamic analysis and optimization of a Stirling cycle for lunar surface nuclear power system," *Appl Therm Eng*, vol. 111, pp. 60–67, Jan. 2017, doi: 10.1016/J.APPLTHERMALENG.2016.08.053.

[7] D. García, M. J. Suárez, E. Blanco, and J. I. Prieto, "Experimental correlations and CFD model of a non-tubular heater for a Stirling solar engine micro-cogeneration unit," *Appl Therm Eng*, 2019, doi: 10.1016/j.applthermaleng.2019.03.013.

[8] Z. Song, J. Chen, and L. Yang, "Heat transfer enhancement in tubular heater of Stirling engine for waste heat recovery from flue gas using steel wool," *Appl Therm Eng*, vol. 87, pp. 499–504, Jun. 2015, doi: 10.1016/j.applthermaleng.2015.05.028.

[9] M. Güven, H. Bedir, and G. Anlaş, "Optimization and application of Stirling engine for waste heat recovery from a heavy-duty truck engine," *Energy Convers Manag*, vol. 180, pp. 411–424, Jan. 2019, doi: 10.1016/j.enconman.2018.10.096.

[10] U. Munir, A. Naeem Shah, S. A. Raza Gardezi, Z. Anwar, and M. S. Kamran, "Oscillatory heat transfer correlation for annular mini channel stirling heater," *Case Studies in Thermal Engineering*, vol. 21, no. May, p. 100664, 2020, doi: 10.1016/j.csite.2020.100664.

[11] L. Rabhi, H. El Hassani, N. Boutammachte, and A. Khmou, “EXAMINATION OF STIRLING ENGINE PARAMETERS EFFECT ON ITS THERMAL EFFICIENCY USING PROSA SOFTWARE,” *Thermal Science*, vol. 27, no. 6, 2023, doi: 10.2298/TSCI220617139R.

[12] J. L. Salazar and W. L. Chen, “A computational fluid dynamics study on the heat transfer characteristics of the working cycle of a β-type Stirling engine,” *Energy Convers Manag*, 2014, doi: 10.1016/j.enconman.2014.08.040.

[13] W. L. Chen, K. L. Wong, and Y. F. Chang, “A numerical study on the effects of moving regenerator to the performance of a β-type Stirling engine,” *Int J Heat Mass Transf*, vol. 83, pp. 499–508, 2015, doi: 10.1016/j.ijheatmasstransfer.2014.12.035.

[14] W. L. Chen, Y. C. Yang, and J. L. Salazar, “A CFD parametric study on the performance of a low-temperature-differential γ-type Stirling engine,” *Energy Convers Manag*, 2015, doi: 10.1016/j.enconman.2015.10.007.

[15] C. H. Cheng and Y. F. Chen, “Numerical simulation of thermal and flow fields inside a 1-kW beta-type Stirling engine,” *Appl Therm Eng*, 2017, doi: 10.1016/j.applthermaleng.2017.04.105.

[16] G. Xiao *et al.*, “Design optimization with computational fluid dynamic analysis of β-type Stirling engine,” *Appl Therm Eng*, 2017, doi: 10.1016/j.applthermaleng.2016.10.063.

[17] A. Abuelyamen, R. Ben-Mansour, H. Abualhamayel, and E. M. A. Mokheimer, “Parametric study on beta-type Stirling engine,” *Energy Convers Manag*, 2017, doi: 10.1016/j.enconman.2017.04.098.

[18] A. K. Almajri, S. Mahmoud, and R. Al-Dadah, “Modelling and parametric study of an efficient Alpha type Stirling engine performance based on 3D CFD analysis,” *Energy Convers Manag*, 2017, doi: 10.1016/j.enconman.2017.04.073.

[19] L. Kuban, J. Stempka, and A. Tyliszczak, “A 3D-CFD study of a γ-type Stirling engine,” *Energy*, vol. 169, pp. 142–159, Feb. 2019, doi: 10.1016/J.ENERGY.2018.12.009.

[20] B. C. Caetano, I. F. Lara, M. U. Borges, O. R. Sandoval, and R. M. Valle, “A novel methodology on beta-type Stirling engine simulation using CFD,” *Energy Convers Manag*, vol. 184, pp. 510–520, Mar. 2019, doi: 10.1016/j.enconman.2019.01.075.

[21] S. A. El-Ghafour, M. El-Ghandour, and N. N. Mikhael, “Three-dimensional computational fluid dynamics simulation of stirling engine,” *Energy Convers Manag*, 2019, doi: 10.1016/j.enconman.2018.10.103.

[22] S. Alfarawi, R. AL-Dadah, and S. Mahmoud, “Influence of phase angle and dead volume on gamma-type Stirling engine power using CFD simulation,” *Energy Convers Manag*, 2016, doi: 10.1016/j.enconman.2016.07.016.

[23] U. Munir, M. Sajid KAMRAN, A. Naeem SHAH, M. Farhan, and Z. Anwar, “CFD METHODOLOGY FOR SIMULATING PUMPING LOSS FROM DISPLACER AND PISTON SEALS OF FREE PISTON STIRLING ENGINE.” Accessed: Nov. 26, 2020. [Online]. Available: http://www.doiserbia.nb.rs/Article.aspx?id=0354-98362000295M

[24] D. Manmohan, “Stirling Space Engine Program,” *Design*, 1999.

[25] E. J. Lewandowski and P. K. Johnson, “Stirling System Modeling for Space Nuclear Power Systems.” 2008. Accessed: Jan. 17, 2019. [Online]. Available: https://ntrs.nasa.gov/search.jsp?R=20080025987

Received: 12.12.2023.
Revised: 06.03.2024.
Accepted: 13.03.2024.